8-19-2010

Cathode Polarizations of a Cathode-Supported Solid Oxide Fuel Cell

Kevin Huang
University of South Carolina - Columbia, huang46@cec.sc.edu

Alessandro Zampieri

Martin Ise

Publication Info

Published in *Journal of The Electrochemical Society*, Volume 157, Issue 10, 2010, pages B1471-B1478.

Publisher's Version: http://dx.doi.org/10.1149/1.3478145
Huang, K., Zampieri, A., & Ise, M. (2010). Cathode Polarizations of a Cathode-Supported Solid Oxide Fuel Cell. Journal of The Electrochemical Society, 157 (10), B1471 - B1478. http://dx.doi.org/10.1149/1.3478145

Journal of The Electrochemical Society, **157** (10) B1471-B1478 (2010)
0013-4651/2010/157(10)/B1471/8/$28.00 © The Electrochemical Society

Cathode Polarizations of a Cathode-Supported Solid Oxide Fuel Cell

Kevin Huang,[a,*,z] Alessandro Zampieri,[b,z] and Martin Ise[b,z]

[a]*Department of Mechanical Engineering, University of South Carolina, Columbia, South Carolina 29208, USA*
[b]*Siemens AG, Corporate Technology, CT T DE HW4 Division, D-91058 Erlangen, Germany*

The concentration, activation, and total polarizations of the cathode in a cathode-supported solid oxide fuel cell (SOFC) were theoretically and experimentally investigated. In the theoretical analysis, the exchange current density of the charge transfer was considered to be dependent on the P_{O_2} determined by the preceding O_2 diffusion, resulting in an interrelationship between activation and concentration polarizations. The established nonlinear polarization equations were then applied to solve the key parameters with area specific resistances and overpotentials of the polarizations experimentally measured by electrochemical impedance spectroscopy on an operating cathode-supported SOFC. To ensure the consistency and meaningfulness of the solutions, the limiting current density in the concentration polarization equation was first solved, followed by the exchange current density of the activation polarization equation using the predetermined limiting current density. The model was finally verified by comparing the directly measured total overpotentials with the calculated ones using the obtained parameters. The agreement between the two favorably supported the proposed cathode polarization model.
 [DOI: 10.1149/1.3478145]

Manuscript submitted April 5, 2010; revised manuscript received July 15, 2010. Published August 19, 2010.

The performance of a cathode-supported solid oxide fuel cell (SOFC) is known to be limited by the cathode and its interface with the electrolyte. It was concluded from an earlier study[1] that over 60% of the total voltage losses of a typical tubular cathode-supported SOFC had association with the cathode at 900°C and that cathode dominance became even greater at lower temperatures. The origins of high cathode polarizations have also been determined to closely relate to the manufacturing process, e.g., high processing temperature needed for achieving gastightness in layers of the electrolyte and the interconnect. The use of high temperature promotes chemical formations of insulating phases such as $La_2Zr_2O_7$ and $SrZrO_3$ at the interface of the electrolyte and the cathode and causes porosity reduction in the substrate, both of which would lead to an increase in cathode polarizations and lowered overall cell performance. In contrast, the NiO–electrolyte composite anode is chemically more compatible with the electrolyte; cosintering of the two at elevated temperatures produces no noticeable chemical reaction. The porosity in the anode is created in situ during operation by the reduction of NiO to Ni and therefore independent of the electrolyte sintering process. More importantly, these unique advantages have ensured to yield excellent performance for anode-supported SOFCs. It also becomes the reason why less and less research efforts have been spent on cathode-supported SOFC development in recent years.

The rise of anode-supported SOFCs, however, does not implicate the end of cathode-supported SOFCs. The cathode-supported SOFCs have demonstrated the longest lifetime among all types of SOFCs (35,000 h at generator level and 50,000 h at single cell level). The merits of cathode-supported SOFCs are best manifested by the geometry of the cathode substrate and its role in the stack design. The tubular geometry of a cathode with one closed end, e.g., Siemens/Westinghouse's, not only avoids the challenging gas seals requirement but also allows for the cell-to-cell connections in reducing atmospheres where inexpensive metals such as Ni can be readily used. The result is the excellent reliability of stack performance. Other types of geometry-substrate variations would have to deal with gas seals (planar anode and planar cathode), chemical reactions (planar cathode), and cell-to-cell connections (tubular anode). Today, high performance but with poor reliability planar anode-supported SOFCs with a metal interconnect stand out to compete with low performance but with good reliability tubular cathode-supported ones for commercialization.

Because the commercialization of the SOFC technology relies upon the coordination of two key elements, cost and reliability, the cathode-supported SOFC maintains its important and solid position in the course of SOFC development. In addition to years' dedicated efforts by Westinghouse and Siemens to develop a product from the tubular cathode-supported SOFC technology, some fundamental research activities in this area can also be found in the literature among the systems of $LaMnO_3$-based/doped ZrO_2 [2-4] and $LaFe(Co)O_3$-based/doped CeO_2.[5,6] In most of these studies, the total cathode polarization was often considered as a sum of irrelevant concentration and activation contributions. A more comprehensive understanding and characterization on the cathode polarizations is still lacking but deemed critical in improving the overall performance of cathode-supported SOFCs.

In this paper, we present through a series of mathematical treatments more general polarization equations depicting coupled charge-transfer and gas-diffusion processes for the cathode of a cathode-supported SOFC. Experimental data such as current-dependent area specific resistances (ASRs) and overpotentials of concentration, activation, and total polarizations obtained from electrochemical impedance spectroscopy (EIS) are particularly utilized to verify the proposed model.

Cathode Polarization Model

Cathode polarizations of a cathode-supported SOFC, like other types of SOFCs, originate from two general sources: ordinary oxygen molecular diffusion through the porous substrate and subsequent charge transfer to reduce oxygen molecules into oxide ions at the interface of the cathode and the electrolyte.

The former diffusion process is typically governed by Fick's laws of diffusion and leads to a voltage loss known as the "concentration polarization." The latter electrode process is generally described by the Butler–Volmer equation and results in the "activation polarization." A simple model depicting the distributions of partial pressure of oxygen (P_{O_2}) across the cathode as well as other functional layers is schematically illustrated in Fig. 1. Two "virtual" layers representing gas diffusion and charge transfer for both the cathode and the anode are particularly shown. Under the open-circuit condition, the P_{O_2} (in dotted lines) at the two electrode/electrolyte interfaces virtually remains the same as those in the corresponding bulk gas streams. No P_{O_2} gradients are present across the cathode and anode layers. However, upon applying an electrical

* Electrochemical Society Active Member.
z E-mail: kevin.huang@sc.edu; alessandro.zampieri@siemens.com; martin.ise@siemens.com

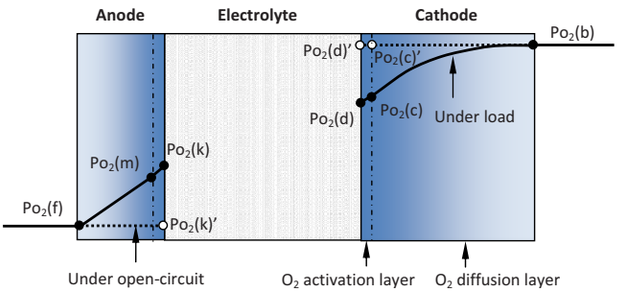

Figure 1. (Color online) Schematic of P_{O_2} distributions across the functional layers of an SOFC. Dashed lines: Under open circuit and solid lines: Under load.

current, $P_{O_2}(c)$ and $P_{O_2}(d)$ at the cathode are lowered, whereas $P_{O_2}(k)$ and $P_{O_2}(m)$ at the anode are elevated, all as a result of the polarization losses. The higher the current applied, the smaller the P_{O_2} gradient across the electrolyte. Because the main interest of this study is in the cathode polarizations, in what follows only cathode-related electrochemical properties are discussed. One of such properties is the partial pressure of oxygen $[P_{O_2}(c)]$ between the two successive cathode polarization layers controlled by the leading O_2 diffusion process. Similarly, $P_{O_2}(d)$ at the electrolyte interface is influenced by the cumulative concentration and activation polarizations. If the activation polarization is described by the Butler–Volmer equation, where the exchange current density i_o is P_{O_2}-dependent, the dependence of i_o on $P_{O_2}(c)$ should be considered in the equation. Therefore, $P_{O_2}(c)$ can serve as a linking parameter to bridge the concentration and activation polarizations in the evaluation of the cathode performance.

Concentration polarization.— The O_2-diffusion induced concentration polarization of a cylindrical tubular porous cathode substrate has been previously studied.[7,8] A geometry-independent, general form of $P_{O_2}(c)$ shown in Fig. 1 as a result of the concentration polarization is given by[7]

$$P_{O_2}(c) = P_t - P_t(1-x)^{1-i/i_L} \quad [1]$$

where P_t is the total system pressure; $x = P_{O_2}(b)/P_t$ is the molar fraction of O_2 in air (0.209); $P_{O_2}(b)$ is the partial pressure of oxygen in bulk air, 0.209 atm at $P_t = 1$ atm; and i and i_L are the current density and limiting current density, respectively. The limiting current density (i_L), at which $P_{O_2}(c)$ becomes zero, is instead a geometry-dependent quantity. For a porous cylindrical tubular cathode,[7] it has the form of

$$i_L = -\frac{\ln(1-x)}{\ln(r_2/r_1)} \times \frac{4FD_{O_2}^{eff}(T)}{RTr_2} \times P_t \quad [2]$$

$$D_{O_2}^{eff}(T) = D_{O_2}(T) \times \frac{\varepsilon}{\tau} \quad [2']$$

where r_2 and r_1 are the outer and inner radii of the cathode tube, respectively, in centimeters; R and F have their usual meanings; $D_{O_2}^{eff}(T)$ is the temperature-dependent effective oxygen diffusivity in cm^2/s; $D_{O_2}(T)$ is the temperature-dependent ordinary O_2 molecular diffusivity in cm^2/s; and ε and τ are the porosity and tortuosity of the porous cathode substrate, respectively. Table I lists the $D_{O_2}(T)$ and $D_{H_2}(T)$ values of some binary gas systems pertinent to SOFCs at representative temperatures, calculated by the dependence of $D_{O_2}(T) \propto T^{1.5}$.[9] To be more accurate, the higher dependence closer to $T^{1.65}$ should also be considered to account for the collision integral Ω. Equation 2′ is used in this study to represent the effective oxygen diffusivity with the ratio of ε/τ as a microstructural factor.

Table I. Calculated D_{O_2} and D_{H_2} values of some SOFC-related binary gas systems.

T (°C)	$D_{O_2}^{O_2N_2}$ (cm^2/s)	$D_{O_2}^{O_2He}$ (cm^2/s)	$D_{H_2}^{H_2H_2O}$ (cm^2/s)
25	0.204	0.743	0.924
800	1.799	6.183	8.294
850	1.947	6.679	8.930
900	2.056	7.162	9.579
950	2.237	7.693	10.248
1000	2.375	8.206	10.937

More comprehensive models with higher fidelity representations of porous-media transport can be found in Ref. 10-14 (just to name a few). In practice, Eq. 2 and 2′ are often applied to either estimate i_L from known microstructural factors (e.g., $m = \varepsilon/\tau$) or to estimate microstructural factors (e.g., ε) from a measured i_L, often with an assumption of $\tau = 1/\varepsilon$ if τ is unknown. In this study, we exercised using this assumption to estimate the porosity of the cathode from a measured i_L. The estimated porosity is listed in Table III.

For a one-dimensional planar geometry, i_L can be further simplified into

$$i_L = -\ln(1-x) \times \frac{4FD_{O_2}^{eff}(T)}{RTt} \times P_t \quad [3]$$

where t is the wall thickness through which the O_2 diffusion takes place. The concentration polarization (η_{conc}) of a solution-based electrochemical system is generally expressed by[15]

$$\eta_{conc} = i\int_0^\infty \left(\frac{1}{\sigma_y} - \frac{1}{\sigma_\infty}\right)dy + \frac{RT}{nF}\sum_k s_k \ln\frac{c_{k\infty}}{c_{ko}} + F\int_0^\infty \sum_j \frac{z_j D_j}{\sigma_y}\frac{\partial c_j}{\partial y}dy \quad [4]$$

where σ_y and σ_∞ are the electrical conductivities of active species in position y to the surface of the electrode and in the electrolyte bulk, respectively; s_k is the stoichiometric coefficient of species k in the electrode reaction; c_{ko} and $c_{k\infty}$ are the concentrations of species k at the electrode surface and the electrolyte bulk, respectively; and z_j and D_j are the charge number and diffusivity of species j, respectively. The first term relates to the ohmic loss due to the conductivity change by diffusion, and the last term refers to the "diffusion potential" caused by the concentration gradient. Applying Eq. 4 to the solid porous cathode through which molecular oxygen diffusion occurs, the first and last terms become zero. Therefore, substitutions of $n = 2$, $s_k = -1/2$, k = O_2, $c \propto P$, and Eq. 1 into Eq. 4 yields the Nernst equation

$$\eta_{conc} = \frac{RT}{4F}\ln\left[\frac{P_{O_2}(b)}{P_{O_2}(c)}\right] = \frac{RT}{4F}\ln\left[\frac{x}{1-(1-x)^{1-i/i_L}}\right] \quad [4']$$

where the electrode reaction is considered as: $1/2\ O_2 + 2e^- = O^{2-}$. This leads to the concentration polarization related ASR (R_{conc}) by differentiating η_{conc} with regard to i at a fixed temperature T

$$R_{conc} = \frac{RT}{4F} \times \frac{\ln(1-x)}{i_L} \times \frac{1}{1-(1-x)^{i/i_L-1}} \quad [5]$$

Clearly, both η_{conc} and R_{conc} follow an exponential dependence on i. The higher the i_L, the lower the polarization. A thinner wall and higher temperature help reduce R_{conc} and η_{conc} in the range of operating current densities. Both Eq. 4′ and 5 can serve as the analytical models for solving i_L from either a measured η_{conc}–i or R_{conc}–i data set. In this study, Eq. 5 is more preferable than Eq. 4′ simply because R_{conc} is a directly measured quantity, whereas η_{conc} is a secondary computed value through integrating the R_{conc}–i data set.

Table II. Attributes of each functional layer in the cathode-supported SOFC studied.

Component	Material	Dimension	Fabrication technique
Cathode	LCM[a]	i.d. 18 mm; o.d. 22 mm	Extrusion
Cathode interlayer	A mixture of LCM and ScSZ[b]	20 μm	Slurry dip coating
Electrolyte	ScSZ	60 μm	Atmospheric plasma spray
Anode	A mixture of Ni and ScSZ	100 μm	Atmospheric plasma spray
Interconnect	Ca- and Al-doped $LaCrO_3$	100 μm	Atmospheric plasma spray
Contact layer	Pure Ni	2 μm	Electroplating
Current collector	Platinum mesh/leads	52 mesh/0.5 mm	Sintered on

[a] Ca-doped $LaMnO_3$.
[b] Sc-doped ZrO_2.

Under one extreme condition, e.g., $i = 0$ (open circuit), the measured R_{conc} can lead to the knowledge of i_L directly from Eq. 5. In the following, i_L is primarily determined from the nonlinear least-square fitting of the R_{conc}–i data set with Eq. 5. The simpler open-circuit approach was not attempted in this study.

Activation polarization.— In classical activation polarization models of the cathode in an SOFC, two elementary steps are generally considered: (*i*) O_2 surface adsorption/dissociation that converts O_2 into reactive oxygen species and (*ii*) charge transfer that converts the reactive oxygen species into oxide ions. In some cases, the surface diffusion of the adsorbed oxygen species should also be considered as one elementary step. Depending on the choice of cathode materials, either or both of them can be rate-limiting. It is generally accepted for $LaMnO_3$-based cathode materials (the same material used in this study), however, that the charge transfer is a slower process than the surface exchange, hence making it the rate-limiting step of the overall cathode kinetics. Furthermore, the rate-limiting charge-transfer step is often associated with single-electron electrode reactions such as[16,17]

$$O_{ad}(s) + e' \xrightarrow{k_f} O'_{ad}(s) \quad [6]$$

where $O_{ad}(s)$ is the adsorbed reactive oxygen species; $O'_{ad}(s)$ and e' represent the negatively charged adsorbed oxygen species and free electrons, respectively; and k_f is the rate constant of the forward charge-transfer reaction (Eq. 6). To use the simplified two-term Butler–Volmer equation to describe the overpotential of the activation polarization, the charge-transfer coefficients of both the anodic and cathodic reactions are assumed to be equal,[18] though it is not necessarily the most accurate[19]

$$\eta_{act} = \frac{RT}{0.5}\sinh^{-1}\left(\frac{i}{2i_o}\right) \quad [7]$$

where i_o (A/cm^2) is the effective exchange current density of the charge-transfer process and in most cases is P_{O_2}-dependent. Zhu et al.[20] derived the following i_o–P_{O_2} relationship by the basic electrode kinetics theory with equilibrium O_2 adsorption/dissociation

$$i_o = i_o^* \times \frac{(P_{O_2}/P^*_{O_2})^{0.25}}{1 + (P_{O_2}/P^*_{O_2})^{0.5}} \quad [8]$$

where i_o^* (A/cm^2) is the intrinsic exchange current density depending on the linear density of the triple-phase boundary and rate constant k_f of the cathodic reaction (Eq. 6) and $P^*_{O_2}$ is a material-dependent constant. Compared to Fig. 1, P_{O_2} in Eq. 8 can be viewed as an equivalent to the interfacial $P_{O_2}(c)$. Substituting Eq. 1 and 8 into Eq. 7 leads to the following i_L-dependent activation polarization overpotential η_{act}

$$\eta_{act} = \frac{RT}{0.5F}\sinh^{-1}\left(\frac{i}{2i_o^*}\left\{\left[\frac{1-(1-x)^{1-i/i_L}}{x^*}\right]^{-0.25} + \left[\frac{1-(1-x)^{1-i/i_L}}{x^*}\right]^{0.25}\right\}\right) \quad [9]$$

where $x^* = P^*_{O_2}/P_t$, a form of molar fraction of oxygen related to $P^*_{O_2}$. There are three independent constants (i_L, i_o^*, and x^*) in the equation. One has to be cautious in attempting to solve the nonlinear equation (Eq. 9) because in many cases, the obtained values are just a set of numbers that meet the optimization criteria of computing algorithm but may not be physically meaningful. To minimize the number of unknown parameters in Eq. 9, the predetermined i_L by solving Eq. 5 with the R_{conc}–i data set is used as a fixed value throughout this study. Therefore, only two parameters (i_o^* and x^*) are left to be solved using the nonlinear equation (Eq. 9) with the η_{act}–i data sets.

Combined cathode polarization.— The sum of Eq. 4′ and 9 gives the total cathode polarization

$$\eta_{tot} = \frac{RT}{0.5F}\sinh^{-1}\left(\frac{i}{2i_o^*} \times \left\{\left[\frac{1-(1-x)^{1-i/i_L}}{x^*}\right]^{-0.25} + \left[\frac{1-(1-x)^{1-i/i_L}}{x^*}\right]^{0.25}\right\}\right) + \frac{RT}{4F}\ln\left[\frac{x}{1-(1-x)^{1-i/i_L}}\right] \quad [10]$$

for P_{O_2}-dependent i_o and the following for P_{O_2}-independent i_o

$$\eta_{tot} = \frac{RT}{0.5F}\arcsin\ h\left(\frac{i}{2i_o}\right) + \frac{RT}{4F}\ln\left[\frac{x}{1-(1-x)^{1-i/i_L}}\right] \quad [10']$$

In the discussions to follow, Eq. 10 and 10′ are used as the model to independently verify the three parameters (i_L, i_o^*, and x^*) obtained from Eq. 5 and 9 by directly comparing the measured and calculated η_{tot} values. The adequacy of the model can be judged by whether an agreement can be reached or not.

In a short summary, the attainment of the three critical electrochemical parameters involves three successive steps: (*i*) using Eq. 5 as the model to solve single constant i_L from the R_{conc}–i data set; (*ii*) using Eq. 9 as the model along with the predetermined i_L to solve the dual constants i_o^* and x^*; and (*iii*) using Eq. 10 with all three constants to calculate η_{tot} and then compare with the measured values.

Experimental

Preparation of testing cells.— The cells used in this study were 11 mm long cutoff segments from a 1.5 m long cylindrical tubular SOFC. The effective surface area of each cell segment is ~5.0 cm^2. Table II summarizes the attributes of each functional layer and their fabrication techniques.

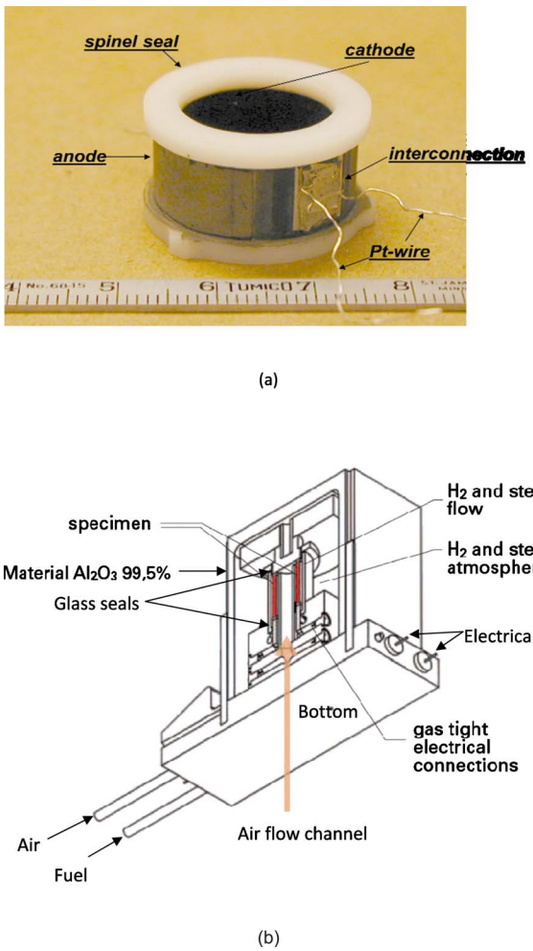

Figure 2. (Color online) Experimental configurations of a cathode-supported tubular cell for EIS measurements. (a) Picture of a unit cell segment and (b) cross-sectional view of the overall testing structure.

A testable SOFC consisted of a cell segment and two MgO/Al_2O_3 spinel collar plates; both of them were prepolished at the ends. The smooth surfaces were necessary to provide platforms for the major gas seals between the mating interfaces. Another thin layer of glass was then employed around the joint to ensure a secondary sealing. A finished unit cell is illustrated in Fig. 2a. The test-cell housing was made of pure alumina and designed with appropriate channels to allow air and fuels to flow separately into the cathode and anode chambers, respectively. Figure 2b shows the cross-sectional schematic view of the overall test-cell configuration. Platinum mesh and leads were used to collect the electrical currents in the reducing atmosphere through the anode and cathode/interconnect.

EIS characterization.— EIS is a choice of methodology for measuring the resistance contributions in different functional layers. In this study, a Zahner IM6 electrochemical workstation was employed to perform the measurements. Its frequency ranges from 10 μHz to 8 MHz with a capability of maintaining up to 3 A of dc bias to the cell. The latter feature is crucial to the present study because it would allow the current density to reach 0.6 A/cm^2 for the current-dependent electrode resistance studies.

A typical measurement sequence can be described as follows. The constructed test-cell assembly is first heated up in a furnace to a desirable temperature with a flowing air and a H_2–H_2O fuel mixture (in 1:1 ratio) exposed to the cathode and anode chambers, respectively. Both air and fuel flows are set to 500 mL/min. After initial stabilization at the measuring temperature, a desirable current is then gradually applied to the cell. The current convention mimics the current flow in a practical SOFC. To assist in separating concentration and activation polarizations, a method known as "He–O_2 shift" is also employed. The basic principle of the method is described in the next section. With the known R_{conc} and the total cathode ASR (R_{tot}) being readily obtained from the spectrum, the activation polarization ASR (R_{act}) can then be taken as R_{tot}–R_{conc}. After the completion of these characterizations, the cell temperature was then changed and the same measurements were repeated. The maximum ranges of temperature and current density varied from 850 to 1000°C and 0 to 0.6 A/cm^2, respectively. Obviously, the instrumentation was more capable of providing a higher current density at higher temperatures due to a lowered overall cell resistance. For repeatability check, each run was conducted on two identical cells in one furnace. The final ASRs were the average values produced from the two cells in each run.

The polarization overpotentials η were obtained from numerically integrating the measured ASRs with respect to i because the exact analytical expressions between them were unknown and usually complex. Specifically, the "trapezoid rule" was applied to perform the numerical integrations.

Helium–oxygen shift.— The method of helium–oxygen (He–O_2) shift is aimed at determining the concentration polarization resistance of a cathode. The principle of this method is based on the fact that the O_2 diffusivity in the He–O_2 mixture is roughly 4 times higher than that in the N_2–O_2 (air) mixture. Therefore, switching air to a mixture of He–O_2 gas at the cathode should reduce the concentration polarization resistance markedly as a result of an enhanced O_2 diffusivity. The selection of 20% O_2 for the He–O_2 mixture was to minimize the effect of P_{O_2} on activation polarization. Furthermore, the P_{O_2} effect on the electrical conductivity of the cathode and ceramic interconnect, both of which are p-type conductors and contribute to the ohmic resistance, could also be avoided. Therefore, the change induced by switching from air to He–20% O_2 reflected largely the change in the concentration polarization of the cathode.

Applying Eq. 5 to air, a mixture of roughly 20% O_2 and 80% N_2, the concentration ASR [R_{conc}(air)] can be written as

$$R_{conc}(\text{air}) = A \times \frac{1}{i_{L,air}} \times \frac{1}{[1-(1-x)^{(i/i_{L,air}-1)}]} \quad [11]$$

$$A = \frac{RT}{4F}\ln(1-x) \quad [12]$$

where $i_{L,air}$ is the limiting current density of cathode in air. A similar equation can also be written for the He–20% O_2 mixture

$$R_{conc}(O_2\text{He}) = A \times \frac{1}{i_{L,O2He}} \times \frac{1}{1-(1-x)^{(i/i_{L,O2He}-1)}} \quad [13]$$

where $i_{L,O2He}$ is the limiting current density of the cathode in He–20% O_2. The difference ΔR_{conc} between R_{conc}(air) and $R_{conc}(O_2\text{He})$, which is experimentally measurable, is obviously given by

$$\Delta R_{conc} = A \times \left[\frac{1}{i_{L,air}} \times \frac{1}{1-(1-x)^{i/i_{L,air}-1}} - \frac{1}{i_{L,O2He}} \times \frac{1}{1-(1-x)^{i/i_{L,O2He}-1}}\right] \quad [14]$$

The significance of Eq. 14 is that the microstructural factor ($m = \varepsilon/\tau$) can be first determined by the measurable ΔR_{conc} at a given i with known theoretical oxygen diffusivities for air and He–20% O_2 (see Table I). The attainment of m can then be utilized to calculate the absolute R_{conc}(air) using Eq. 11 with assumed constant m. For convenience, Ref. 21 lists a number of tables in Appendix 3 and plots several graphs under a few representative conditions to facili-

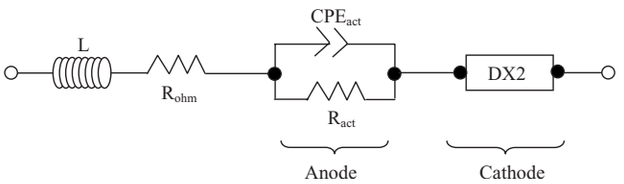

Figure 3. Equivalent electrical circuit used in this study for simulating the measured impedance spectra from a cathode-supported SOFC.

tate the simultaneous attainments of m and R_{conc}(air) from a measured ΔR_{conc}. In this study, all R_{conc} values were obtained by the above-described He–O_2 shift method.

Equivalent circuit.— The collected impedance spectra were analyzed with ZView (version 2.8, Scribner Associates) with its built-in equivalent circuits. Figure 3 shows the equivalent electrical circuit used in this study. The element DX2 (DX11-Bisquert #2) was selected from the library of ZView equivalent circuits to simulate the cathode polarization process because the two-phase composite network present in the cathode can be better represented by a chain-conductor model. For the anode polarization, only one charge-transfer process, namely activation polarization, was represented by one R-CPE parallel circuit because the concentration polarization of the anode is negligible for the cathode-supported SOFC. CPE (constant phase element) is a general form of impedance that covers from pure resistors to pure capacitors. All ohmic contributions from the different functional layers were lumped into R_{ohm}. To account for the inductance effect caused by the measuring wires, an inductor was also included in the circuit model.

Results and Discussion

Identification of cathode polarization process.— The first step to determine the cathode ASRs from an impedance spectrum measured from an SOFC is to identify which semicircle (or arc) corresponds to the cathode kinetics. A representative impedance spectrum of an operating cathode-supported SOFC is shown in Fig. 4. It features two distinct semicircles (or arcs) spreading across the frequency domain on a complex plane with the smaller one at higher frequency and the large one at lower frequency. To determine which one is cathode-related, the aforementioned He–O_2 shift method was employed. It is evident from Fig. 4 that a marked reduction in ASR

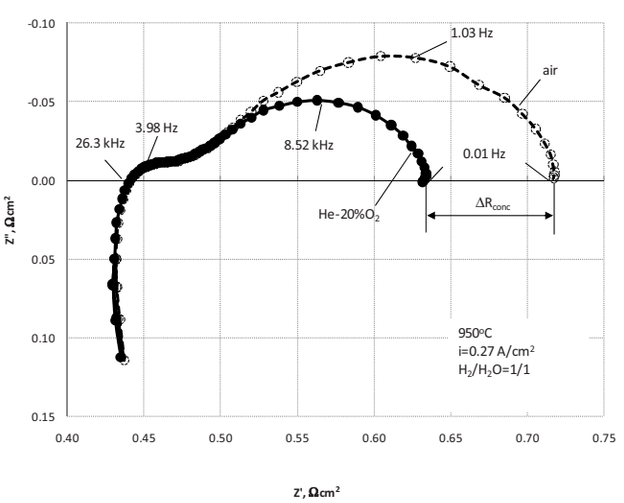

Figure 4. A representative impedance spectrum measured from an operating cathode-supported SOFC. The dotted semicircle represents the spectrum using air as the oxidant and solid semicircle represents the spectrum using He–20% O_2 as the oxidant.

only occurs at the low frequency semicircle after the oxidant is switched from air to the He–20% O_2 mixture while the fuel composition is kept the same. The implications of such an ASR reduction are threefold. First, it identifies that the low frequency semicircle is indeed associated with the cathode kinetics. The high frequency semicircle has been previously identified to be related to the anode kinetics in a Siemens' internal study,[22] in which the only semicircle that responded to the anode gas change was the first high frequency one. Second, the degree to which the ASR is shrunk by switching oxidants with the same concentration of O_2 mainly reflects the change in R_{conc} with a marginal influence on R_{act}. Third, it allows for a quantitative determination of R_{conc} from Eq. 14, and R_{act} can be further determined as R_{tot}–R_{conc}. The rationality of the above identification is also understandable in that the insignificant anode polarization of a cathode-supported SOFC signals a higher exchange current density and a negligible H_2 diffusion-related concentration polarization (very thin anode layer and higher H_2 diffusivity) for the fuel oxidation and therefore should appear at a high frequency range. In contrast, the slower cathode kinetics with smaller exchange current density and larger O_2 diffusion related concentration polarization (very thick cathode layer and relatively lower O_2 diffusivity) should mainly occupy the low frequency domain of the spectrum. It is further estimated from the peak frequencies shown in Fig. 4 that the time constant for the anode kinetics is $\sim$19 μs, whereas the time constants for the cathode kinetics are 155 ms with air and 40 ms with He–20% O_2, respectively. The magnitudes of the time constants for the anode and cathode semicircles place the anode and cathode kinetics in the charge-transfer and gas-diffusion regimes, respectively. The following results evidently support this assertion.

Cathode ASRs vs current density.— With the separation of the cathode-related ASRs, Fig. 5 plots the individual ASR of (a) total, (b) concentration, and (c) activation polarizations as a function of current density at four temperatures. At first glance, one can easily capture the similarity in the R_{tot}–i and R_{conc}–i curves, e.g., a slow increase at low current density followed by a pronounced increase at high current density (lack of high current density data points for 900 and 850°C prevents showing the sharp increase). Different from the R_{tot}–i and R_{conc}–i curves, the R_{act} in Fig. 5c displays its own dependence on i at different temperatures, e.g., flat at 1000°C, slight increase at 950 and 900°C, and slight decrease at 850°C. The opposite trending between R_{act}–i and R_{conc}–i at 850°C seems to cancel out to yield a flat R_{tot}–i curve in the current density range plotted.

The similarity between R_{tot}–i and R_{conc}–i curves at 950 and 1000°C is an indication of the domination of cathode polarization by R_{conc}. This is also supported by the fact that the magnitude of R_{conc} is markedly greater than R_{act}, and the degree to which R_{conc} varies with i is appreciably larger at these two higher temperatures. The R_{conc} dominance with temperature is primarily ascribed to the difference in the activation energies of the charge-transfer and gas-diffusion processes, i.e., the charge-transfer process is more temperature-sensitive (or higher activation energy) than the gas-diffusion (projected $i_L \propto T^{0.5}$). At the lower temperature (850°C), the overall cathode polarization is dominated by R_{act} as is evidenced not only by the high R_{act} values shown in Fig. 5c but also by the decrease in R_{act} with i. The latter is a characteristic of the Butler–Volmer equation (Eq. 7) as the slope of $(\partial\eta_{act}/\partial i)$ decreases with increasing i.

The importance of Fig. 5b is that it provides a theoretical foundation for using experimental data to solve i_L. The lines shown in the figure represent the nonlinear least-square fittings of the measured values using DataFit software (version 9.0, Oakdale Engineering). The fittings are generally good, except for one data point at $i = 0.50$ A/cm^2 and 950°C. The obtained i_L at different temperatures are listed in the second column of Table III; it is used as the fixed value for subsequent simulations. Along with i_L values, the corresponding effective oxygen diffusivities and substrate porosity calculated by assuming $\tau = 1/\varepsilon$ are also listed in Table III. The

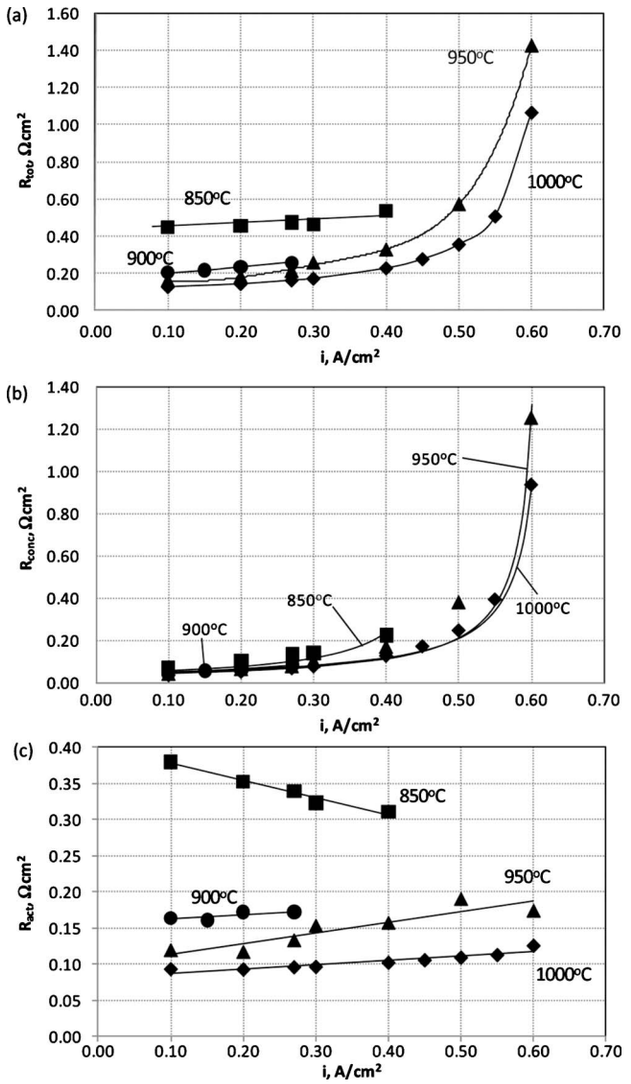

Figure 5. Cathode-related ASRs of polarization as a function of current density at four different temperatures: (a) Total, (b) concentration [lines representing fittings with Eq. 5], and (c) activation.

porosity remains reasonably constant with temperature as it should be. To further support the obtained porosity values, Fig. 6 shows the microstructure of a Siemens/Westinghouse cathode substrate before electrolyte densification. The average porosity is estimated to be ~33%. A following densification of the electrolyte at 1345°C further reduces the porosity to below 30%, which agrees well with the values in Table III. To verify the dependence of i_L on temperature as suggested by Eq. 2, the obtained i_L is plotted against $T^{0.5}$ and shown

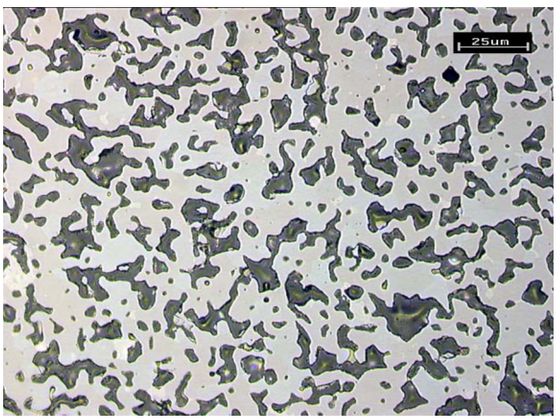

Figure 6. (Color online) A plot of i_L as a function of $T^{0.5}$.

in Fig. 7. A stronger dependence than that predicted as $i_L \propto T^{0.5}$ in Eq. 2 is probably an indication of the effect of He–20% O_2 on R_{act} as well as a coupled relationship between R_{act} and R_{conc}.

Activation polarization vs current density.— The overpotentials of activation polarization (η_{act}), numerically integrated from R_{act}, are plotted in Fig. 8 as a function of i for four temperatures. Along with the data points are solid lines representing nonlinear least-square fitting using Eq. 9 as the model and the predetermined i_L as a fixed value. The model appears to predict an upward bending at $i > 0.50$ A/cm^2 for 950 and 1000°C where $i > 0.50$ A/cm^2 data points are available. Also plotted in dotted lines are the simulations using Eq. 7 as the model, in which i_o is considered to be independent of P_{O_2}. The difference begins to be noticeable at higher i, e.g., >0.50 A/cm^2. This trend appears to suggest a more pronounced P_{O_2} dependence of i_o at higher current densities. The outcomes of solving nonlinear Eq. 9 are the two best fit parameters i_o^* and x^*. They are listed in the fifth and sixth columns of Table III, respectively. There is no apparent trending among x^* values with temperature, particularly the value at 900°C, which could be caused by insufficient data points. In all cases, the obtained x^* values are small, implying a large but temperature-insensitive equilibrium constant for the adsorption/desorption reaction ($P_{O_2}^* = 1/K$, see Ref. 20). The concentration of the surface adsorbed oxygen species is high and well-equilibrated. They are also quite different from those reported by Matsuzaki and Yasuda[23] on a Pt/8YSZ (where YSZ is yttria-stabilized zirconia) system. The different cathode materials could account for the disagreement. For comparison, the last column also lists the i_o values obtained from solving Eq. 7. These values are comparable to those reported in Ref. 24 (e.g., 0.450 A/cm^2 at 900°C) where the $La_{0.6}Sr_{0.4}MnO_3$–YSZ cathode was investigated by the ac impedance technique. An Arrhenius plot of i_o^* and i_o given in Fig. 9 reveals an almost identical activation energy of E_a = 1.197 eV between the two, suggesting that $P_{O_2}(c)/P_{O_2}^*$ is rela-

Table III. Best fit parameters obtained from nonlinear least-square fittings of various models indicated.

	From Eq. 5 and 2			From Eq. 9		From Eq. 7
T (°C)	i_L (A/cm^2)	$D_{O_2}^{eff}$ (cm^2/s)	ε	i_o^* (A/cm^2)	x^*	i_o (A/cm^2)
1000	0.629 ± 0.001	0.160	0.26	2.301 ± 0.025	0.056 ± 0.010	1.120 ± 0.010
950	0.621 ± 0.001	0.152	0.26	1.611 ± 0.044	0.089 ± 0.027	0.752 ± 0.023
900	0.560 ± 0.017	0.131	0.25	1.130 ± 0.040	0.608 ± 0.236	0.526 ± 0.004
850	0.499 ± 0.010	0.112	0.24	0.509 ± 0.001	0.068 ± 0.006	0.253 ± 0.001

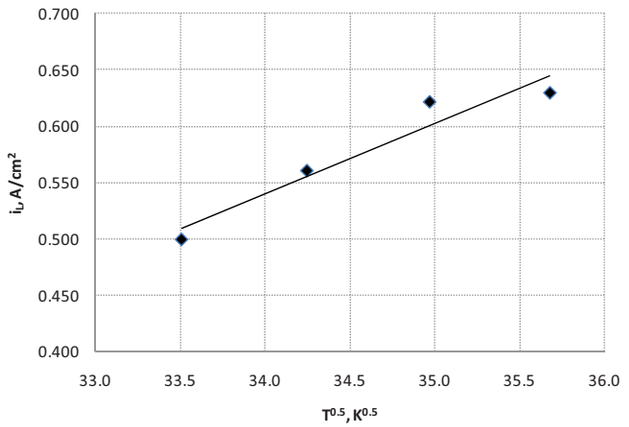

Figure 7. (Color online) A representative microstructure of the cathode substrate before the electrolyte densification.

tively constant. The underlying reason is unclear at this point and will be investigated in a future study. The high E_a suggests that the charge transfer is indeed a strongly temperature-sensitive process as pointed out earlier.

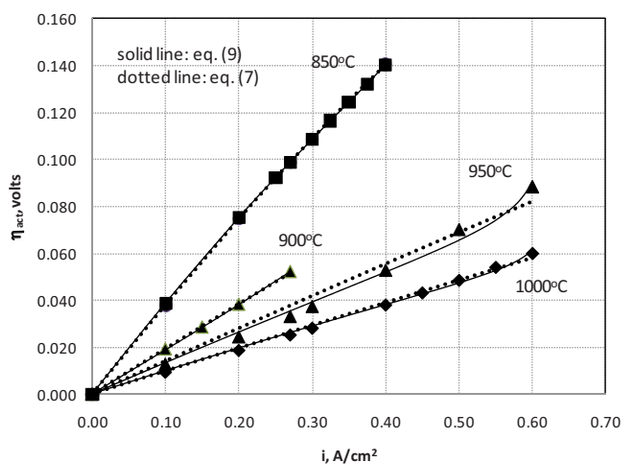

Figure 8. (Color online) Activation polarization of cathode as a function of current density at four different temperatures along with nonlinear least-square fitting with Eq. 9 and 7 as the models.

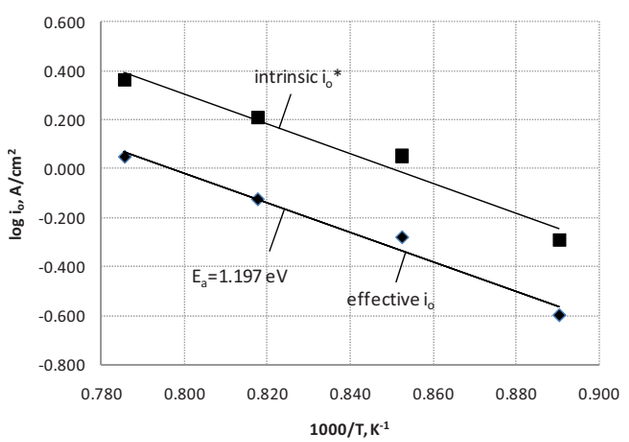

Figure 9. (Color online) Arrhenius plots of effective and intrinsic exchange current densities of the cathode.

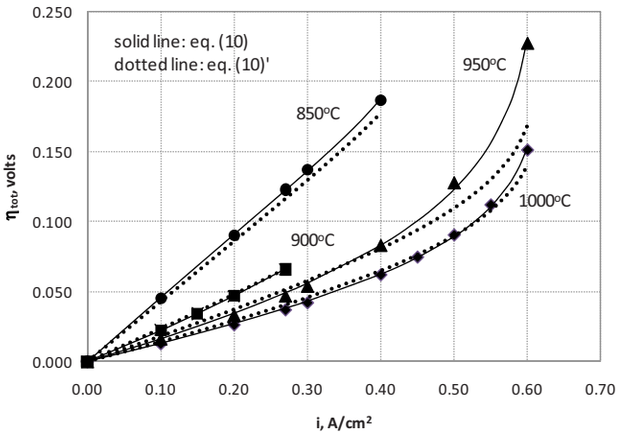

Figure 10. (Color online) Total polarization of cathode as a function of current density at four different temperatures along with nonlinear least-square fittings using Eq. 10 (solid lines) and Eq. 10′ (dotted lines) as the models.

Total polarization vs current density.— To verify the model, the numerically integrated total polarizations η_{tot} as a function of i at four temperatures are shown in Fig. 10. R_{tot}, from which η_{tot} is derived, is determined with the highest accuracy as a result of direct reading from the spectrum. The solid and dotted lines represent the simulations using Eq. 10 and 10′ as the models, respectively, and the corresponding parameters listed in Table III. It is evident that the use of Eq. 10 produces the best fit to the measured data points, whereas the use of simplified Eq. 10′ yields deviations at higher current densities. Therefore, it is reasonable to conclude that the proposed coupled polarization model is a more general representation over a broader range of current density. It also becomes much clearer in Fig. 10 than in Fig. 8 that the effect of P_{O_2} on i_o begins to play a significant role at higher current densities.

Conclusions

The total cathode polarization of a cathode-supported SOFC has been considered in this study as a result of two interrelated contributions: concentration polarization of O_2 diffusion and activation polarization of charge transfer. The leading O_2 diffusion is shown to determine the P_{O_2} that would affect the subsequent charge transfer. With this P_{O_2} as the linking parameter, polarizations of concentration and activation are coupled. The conventional EIS technique in conjunction with the He–O_2 shift method is employed to experimentally separate R_{conc} from R_{tot}. This allows for the attainment of i_L, which is used as a fixed value for subsequent simulations and verification of the model by fitting R_{conc}–i data. The obtained i_o and i_o^* share an almost identical activation energy at a higher level, indicating a strong temperature-dependent charge-transfer process. The i_o^* and x^* obtained by solving the nonlinear equation (Eq. 9) with the η_{act}–i data set and the predetermined i_L are also applied to calculate η_{tot} using Eq. 10. The excellent agreement between the measured and calculated values favorably confirms the proposed polarization model. The model is more suitable for a broader range of current density. Overall, the cathode performance of the Siemens/Westinghouse cathode-supported SOFCs is mainly dominated by oxygen diffusion, especially at higher current density for temperatures greater than 900°C, below which it is largely limited by the charge-transfer polarization.

Acknowledgment

The authors thank the U. S. Department of Energy and the German BMWi for financial support of the project under the agreements of DE-FC-02NT41247 and 0327078B, respectively. B. Schricker,

M. Brasse, P. Ritzer and P. Muhl are specially thanked for their technical support.

University of South Carolina assisted in meeting the publication costs of this article.

References

1. K. Huang, in *Proceedings of the Seventh European Solid Oxide Fuel Cell Forum*, European Fuel Cell Forum, Lucerne, p. P0303 (2006).
2. J. Chen, Q. L. Liu, S. H. Chan, N. P. Brandon, and K. A. Khor, *Electrochem. Commun.*, **9**, 767 (2007).
3. K. Yamahara, C. P. Jacobson, S. J. Visco, and L. C. De Jonghe, *Solid State Ionics*, **176**, 452 (2005).
4. H. Orui, K. Watanabe, and M. Arakawa, *J. Power Sources*, **112**, 90 (2002).
5. Y. Liu, S. Hashimoto, H. Nishino, K. Takei, and M. Mori, *J. Power Sources*, **164**, 56 (2007).
6. M. Liu, D. Dong, F. Zhao, J. Gao, D. Ding, X. Liu, and G. Meng, *J. Power Sources*, **182**, 585 (2008).
7. K. Huang, *J. Electrochem. Soc.*, **151**, A716 (2004).
8. K. Huang, *J. Electrochem. Soc.*, **151**, E256 (2004).
9. J. R. Welty, C. E. Wicks, R. E. Wilson, and G. Rorrer, *Fundamentals of Momentum, Heat, and Mass Transfer*, 4th ed., p. 432, John Wiley & Sons, New York (2001).
10. E. A. Mason and J. A. Malinauskas, *Transport in Porous Media: The Dusty-Gas Model*, Elsevier, New York (1983).
11. G. F. Froment and K. B. Bischoff, *Chemical Reactor Analysis and Design*, John Wiley & Sons, New York (1990).
12. R. Krishna and J. A. Wesselingh, *Chem. Eng. Sci.*, **52**, 861 (1997).
13. R. Suwanwarangkul, E. Croiset, M. W. Fowler, P. L. Douglas, E. Entchev, and M. A., Douglas, *J. Power Sources*, **122**, 9 (2003).
14. Y. Vural, L. Ma, D. B. Ingram, and M. Pourkashanian, *J. Power Sources*, **195**, 4893 (2010).
15. J. Newman and K. E. Thomas-Alyea, *Electrochemical Systems*, 3rd ed., p. 493, John Wiley & Sons, New York (2004).
16. A. C. Co and V. I. Birss, *J. Phys. Chem. B*, **110**, 11299 (2006).
17. J. D. Kim, G. D. Kim, J. W. Moon, Y. I. Park, W. H. Lee, K. Kobayashi, M. Nagai, and C. E. Kim, *Solid State Ionics*, **143**, 379 (2001).
18. D. A. Noren and M. A. Hoffman, *J. Power Sources*, **152**, 175 (2005).
19. F. H. van Heuveln and H. J. M. Bouwmeester, *J. Electrochem. Soc.*, **144**, 134 (1997).
20. H. Zhu, R. J. Kee, V. M. Janardhanan, O. Deutschmann, and D. G. Goodwin, *J. Electrochem. Soc.*, **152**, A2427 (2005).
21. K. Huang and J. B. Goodenough, *Solid Oxide Fuel Cell Technology: Principles, Performance and Operations*, p. 166, Woodhead, Cambridge, United Kingdom (2009).
22. M. Ise, Siemens Internal Technical Report, PS4/D1AL/0466, Siemens (2004).
23. Y. Matsuzaki and I. Yasuda, *Solid State Ionics*, **126**, 307 (1999).
24. A. C. Co, S. J. Xin, and V. I. Birss, *J. Electrochem. Soc.*, **152**, A570 (2005).